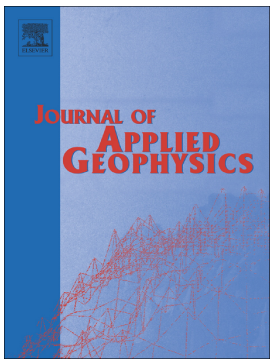

Geophysical response to simulated methane migration in groundwater based on a controlled injection experiment in a sandy unconfined aquifer

Dylan R. Klazinga, Colby M. Steelman, Anthony L. Endres, Beth L. Parker

PII: S0926-9851(18)31035-8
DOI: https://doi.org/10.1016/j.jappgeo.2019.05.019
Reference: APPGEO 3784

To appear in: *Journal of Applied Geophysics*

Received date: 7 December 2018
Revised date: 27 May 2019
Accepted date: 29 May 2019

Please cite this article as: D.R. Klazinga, C.M. Steelman, A.L. Endres, et al., Geophysical response to simulated methane migration in groundwater based on a controlled injection experiment in a sandy unconfined aquifer, Journal of Applied Geophysics, https://doi.org/10.1016/j.jappgeo.2019.05.019

Geophysical response to simulated methane migration in groundwater based on a controlled injection experiment in a sandy unconfined aquifer

Dylan R. Klazinga[1,2], Colby M. Steelman[1,3,*] cmsteelman@uwaterloo.ca; csteelma@uoguelph.ca, Anthony L. Endres[1], Beth L. Parker[3]

[1]Department of Earth and Environmental Sciences, University of Waterloo, Waterloo, Ontario, Canada
[2]Sensors and Software Inc., Mississauga, Ontario, Canada
[3]G[360] Institute for Groundwater Research, College of Engineering and Physical Sciences, University of Guelph, Guelph, Ontario, Canada

[*]Corresponding author.

Abstract

Geophysical methods have the capacity to detect and characterize gas-phase dynamics in groundwater. Suitable methods can be deployed at surface or within boreholes depending on the required depth of investigation, spatial/temporal resolution, and geologic conditions. While the application of geophysical methods to monitor immiscible phase contaminants in the subsurface has been extensively documented, the effects of hydraulic properties and flow system conditions on the nature of the geophysical responses used to elucidate multi-phase fluid flow remains underdeveloped. A series of numerical 2-dimensional multi-phase flow and geophysical model simulations based on a controlled methane release experiment in the Borden unconfined sand aquifer was carried out to assess the influence of porous media hydraulic properties and flow system conditions on geophysical signatures associated with transient gas-phase saturation and gas migration behaviour. Therefore, the utility of electrical resistivity tomography (ERT) and ground-penetrating radar (GPR) to monitor gas-phase plume dynamics in shallow groundwater flow systems is examined. ERT and GPR responses to gas-phase distribution and migration during a 72-day methane gas injection and subsequent recovery period was calculated using a numerical multi-phase flow model (CFbio) simulating four distinct parameterizations of the sandy aquifer system. Geophysical models showed that ERT was effective at imaging the central position of the plume but was less effective at detecting thinner lateral migration pathways extending beyond the primary high gas saturation bulb. Conversely, GPR was able to detect thin gas pools emanating from the primary gas bulb and small-scale vertical preferential pathways arising from capillary boundaries with contrasting saturations; however, gradational boundaries proved to be more difficult to resolve using GPR. This study demonstrates that ERT and GPR can be very useful tools in combination for longer-term monitoring of stray gas leakage from decommissioned hydrocarbon wells in shallow granular media freshwater aquifers, especially given the likelihood of strong lateral migration.

1.0 Introduction

The behaviour of methane gas in petroleum reservoirs has been studied for decades (Perrodon, 1983); however, much less is known about the impacts of stray gas in shallow, freshwater aquifers, particularly those used as a drinking water supply (Cahill et al., 2018). Fugitive methane emanating from a compromised well bore will generally flow upwards due to buoyancy, potentially leading to groundwater contamination (Osborn et al., 2011; Schout et al., 2018). It has recently been shown that even subtle heterogeneity and anisotropy in sedimentary formations can lead to significant lateral gas migration (Cahill et al., 2017), leading to complex distributions in hydrogeologic systems (Moortgat et al., 2018). Therefore, better tools are needed for monitoring its migration and assessing impacts on groundwater quality (Vidic et al., 2013) and public health and well-being (Royal Society, 2012; Council of Canadian Academies, 2014).

Geophysical methods represent a powerful tool in the detection of groundwater contaminants and have been applied to a wide range of immiscible-phase liquid studies over the past 30 years (e.g., Brewster and Annan, 1994; Brewster et al., 1995; Daily and Ramirez, 1995; Tomlinson et al., 2003; Hwang et al., 2008). Geophysics exploits differences in fluid-phase physical properties that are associated with hydrologic processes or dynamic systems (e.g., Boaga, 2017). Some of the most commonly measured properties include dielectric permittivity using ground-penetrating radar (GPR) and electrical resistivity or conductivity using direct current electrical methods such as electrical resistivity tomography (ERT). When a contaminant is introduced to a saturated volume, it will variably displace, mix and dissolve with the existing fluids, causing a change in the bulk geophysical properties. These changes can be measured over time to determine the spatial extent and temporal evolution of the contaminant and associated biogeochemical processes (Knight et al., 2010; Atekwana and Atekwana, 2010; Binley et al., 2015).

Geophysical measurements are often used to aid spatial and temporal interpretations of high-resolution geologic and hydrogeologic datasets, such as those obtained from continuous cores, geochemical sampling, and depth-discrete hydraulic testing (e.g., Meyer et al., 2016; Harvey et al., accepted). Relative to direct geologic and hydrological measurements, geophysical data is inherently non-unique potentially resulting in limited interpretability; however, integration of high-resolution geologic and hydrogeologic datasets with geophysical measurements can strengthen deterministic characterizations of complex processes.

A controlled methane injection experiment at Canadian Forces Base (CFB) Borden by Cahill et al. (2017) was conducted to better understand subsurficial methane migration and its impact on groundwater. Over a period of 72 days, a total of 51.35 m^3 of methane gas was injected into the sandy unconfined aquifer. Using a combination of hydrogeological, geophysical, and geochemical methods, the migration of methane was tracked within the aquifer (Steelman et al., 2017; Cahill et al., 2018) and vadose zone (Forde et al., 2018). Cahill et al. (2017) concluded that approximately half of the gas vented to the atmosphere during the 72-day active injection period, while the other half migrated laterally in the direction of groundwater flow and persisted in the groundwater for an extended period (>1 year). Although a portion of the gas effluxed to the atmosphere, groundwater samples together with surface GPR measurements collected during the active injection phase indicated that a substantial portion of the methane gas remained entrapped in the groundwater beneath stratigraphic layers, resulting in a persistent, yet dynamic dissolved methane plume (Cahill et al., 2018).

Time-lapse GPR and ERT measurements collected during the active injection phase was used to delineate the extent of methane gas migration in the aquifer (Steelman et al., 2017). This geophysically delimited gas plume was supported by increases in the total dissolved gas pressure

measured within the aquifer. Three major temporal peaks in gas accumulation were noted in the radargram time-series (Days 8, 37, and 65) revealing a series of transient gas build-ups followed by large lateral gas migration events. The largest increase in GPR reflectivity was observed between Days 51 and 72. Based on these geophysical data, the methane travelled farther down-gradient than expected based on groundwater advection alone. Following these pressure release events, gas was observed to accumulate at pre-existing reflectors corresponding to lithologic boundaries due to measured contrasts in grain size along horizontal layers creating subtle contrasts in hydraulic permeability. After the gas injection was stopped, the reflectivity of these reflectors diminished over time due to reduced gas-phase saturations by buoyancy driven migration and/or dissolution into the groundwater.

Steelman et al. (2017) demonstrated the capacity of surface geophysics to track the transient behaviour of methane gas migration in shallow aquifers. The authors of the study concluded that heterogeneity and horizontal to vertical anisotropy in hydraulic parameters strongly controlled the lateral migration pathways, including the periodic gas build-up and release events. Field observations revealed that gas migration extended much farther down-gradient than expected from advection alone and occurred through a series of rapid lateral migration events irrespective of changes in the injection rate. However, the exact role of the sedimentary structures and their properties (e.g., permeability, capillary pressure, geometry) on the geophysical signatures used to elucidate the migration and behaviour of the gas in the aquifer was not fully delineated at the experimental site. Perhaps the most interesting observation from this experiment was the relationship between gas bulb formation near the injectors revealed by ERT, followed by a sudden lateral migration of the gas-phase along centimetre-scale bedding or sedimentary laminations revealed by GPR measurements.

Several conclusions were drawn from the geophysical measurements collected during the field experiment. It was observed that the gas-phase is highly mobile and laterally extensive in groundwater; lateral gas migration is much faster and extends farther than that predicted by advection alone; the gas-phase preferentially accumulates beneath subtle permeability contrasts or grain-scale bedding features; and the gas exhibited periodic ebullition events resulting in sudden lateral and vertical migration in the aquifer. Although GPR and ERT measurements yielded convincing evidence of gas-phase migration and redistributions in the aquifer, the cumulative impacts of physical properties and flow system conditions on the evolution of the gas-phase plume and corresponding geophysical responses were not fully understood.

The aim of this current study is to assess the influence of porous media hydraulic properties and flow system conditions on the geophysical signatures associated with transient gas-phase saturation and gas migration behaviour observed in the unconfined Borden aquifer. Here, two-dimensional (2D) numerical multi-phase flow and geophysical model simulations were used to evaluate how sedimentary bedding with varying lateral continuity, permeability and capillary pressure relationships due to pore-scale variability, influences the geophysical signatures associated with the presence, accumulation, and migration of gas in an unconfined sandy aquifer with Borden aquifer properties. This is achieved through a series of idealized multi-phase flow model scenarios that capture the main physical elements believed to be contributing to the geophysical signatures and interpreted hydrogeological characteristics of the gas-phase plume in the Borden aquifer, which has been well characterized with over 40 years of hydrogeological experiments published in the literature (Sudicky and Illman, 2011). Four basic scenarios were tested based on a range of physical properties and aquifer-aquitard geometries informed by data collected during the field experiment. These flow scenarios were used to develop geophysical

models to assess the cumulative impacts of subsurface properties on the geophysical response observed during the field experiment (Steelman et al., 2018). Here, gas distributions were converted to equivalent dielectric permittivity and resistivity distributions using established petrophysical relationships. In this way, the multi-phase flow models were used as an input for modelling the geophysical response observed in the ERT and GPR data. Our numerical results provide a comparison of the relative sensitivity of GPR and ERT to changes in porewater saturation as a function of the physical conditions of the aquifer during a variable rate methane injection experiment scenario described by Cahill et al. (2017), thereby providing insights into the utility of geophysical methods for the detection of methane leakage from a compromised wellbore in a shallow groundwater flow system, i.e., a real-world scenario.

2.0 Methods

2.1 Multiphase Flow Modelling

2.1.1 Conceptual Framework

CompFlowBio (CFbio) (Forsyth and Shao, 1991; Unger et al., 1995) was selected to complete the methane flow numerical modelling. The program uses a first-order accurate, finite-volume formulation to solve a series of differential equations for the conservation of contaminant, water, and air. Modelling began with the definition of a base case, informed by data retrieved during the field experiment at CFB Borden (Cahill et al., 2017). Grain size analysis and permeameter testing of the sediment samples from core taken at 5 cm lengths revealed a four-layer system (Steelman et al., 2017). The first three layers were dominated by fine to coarse sands (94 to 99%) with high permeabilities ($k \approx 1 \times 10^{-12}$ m^2). The second layer was less well-sorted and had a higher percentage of coarse sands, pebbles, silts and sands, and a permeability approximately one

order of magnitude lower than the first and third layers. The fourth layer beginning at a depth of approximately 7.4 m bgs, represented the transition to the aquitard which was effectively located at 9.0 m bgs. This lowermost layer and was characterized by a higher percentage of silts and clays (17%) with low permeability ($k \approx 1 \times 10^{-14}$ m^2).

The base scenario consists of an unconfined aquifer over an aquitard (Figure 1). The first layer was an amalgamation of the upper three layers with a lateral permeability (k_h) of 2.2×10^{-12} m^2 and a porosity (ϕ) of 0.33. The second layer represented the aquitard, $k_h = 6.4 \times 10^{-14}$ m^2 and $\phi =$ 0.39. Soil compaction and vibration of the core resulted in highly variable, and thus, unreliable estimates of porosity; therefore, literature values for porosity of the Borden sand were used in these models (Das, 2008). The boundary between the aquitard and the aquifer was set at 9.0 m bgs; both the aquifer and aquitard had an anisotropy ratio of $k_h/k_v = 10$.

Boundary conditions were set to maintain a 1.0 m depth to the water table, directly above the injectors placed at 4.5 and 9.0 m bgs, with an average linear groundwater velocity of 6 cm/day in the aquifer; the pressure was defined at the lower two corners of the model domain, creating a horizontal hydraulic gradient of 0.0106 m/m with a constant head boundary along the base and along the right and left sides of the domain. The upper boundary, representing the atmosphere, was defined by a pressure of 100 kPa and given a constant recharge rate of 0.7 mm/day. At initialization, the model was fully saturated below a depth of 0.7 m bgs and was 60% saturated above 0.7 m bgs. The model was run for 100 days prior to the start of the injection to reach steady state condition.

Relative permeability was determined using the Brooks-Corey parameters from Kueper and Frind (1991): an entry pressure (P_c) of 2.22 kPa; residual saturation ($\theta_{w,r}$) of 0.078; and a pore

size distribution index (λ) of 2.48. A residual gas saturation of 10% was assumed. The free-phase flow modelling accounted for neither aerobic nor anaerobic degradation of the methane; nor geochemical reactions caused by the presence of the methane. Since these simplifications were included in the free-phase flow model, they were inherited by the geophysical modelling. Hence, changes in the geophysical properties along the mineral grain surface were not considered when determining the geophysical response of the gas distribution. Furthermore, the influence of temperature on the viscosity, dielectric permittivity, and electrical conductivity, as well as precipitation, evapotranspiration, and barometric pressure were considered negligible and ignored.

The injector geometry was modelled after the actual injector geometry of the experiment (Figure 1) (Cahill et al., 2017). Gas injectors were placed at 4.5 m and 9.0 m bgs, 8 m from the up-gradient boundary. A four stage stepped injection rate was used (Figure 2): a slow injection rate (Phase I: 2 × 0.06 L/min), a moderate injection rate (Phase II: 2 × 0.35 L/min), a moderate injection from the deeper well only (Phase III: 1 × 0.35 L/min), and a fast injection (Phase IV: 2 × 1.5 L/min). A temporary shut-down of the injectors was included during Phase II between Days 38 – 44 as per the field experiment. The injectors were modelled as point sources during Phases I – III, while distributed injectors were used during Phase IV to accommodate model instability due to the high volume of gas being added to the system. The distributed injectors were 0.3 m tall and 0.2 m wide with their base centred on the location of the previous point source injectors.

3.1.2 Flow Model Parametrization

A 2D model domain of dimension 10 m × 20 m provided an adequate balance of model accuracy and computation time. A depth of 10 m was used as a negligible response was expected 1 m below the top of the aquitard. The model was discretized in a 0.1 m × 0.1 m grid. The convergence tolerances for the majority of the model time were 1×10^{-4} kPa for pressure, 1×10^{-5} for saturation, 1×10^{-7} for the mole fraction of methane, and 1×10^{-2} K for temperature. During Phase IV, the increased injection rate made it difficult for CFbio to converge, so the tolerances were changed to 5×10^{-3} kPa for pressure, 5×10^{-4} for saturation, 5×10^{-6} for the mole fraction of methane, and 5×10^{-2} K for temperature.

3.1.3 Modelled Scenarios

Following the definition of the base case (*Scenario A*) modifications were applied to investigate the impacts of varying hydraulic parameters and geometries on the geophysical response of free-phase methane migration (*Scenario B, C* and *D*) (Figure 1). In total, four scenarios were used to investigate the geophysical responses observed during the injection. Each scenario represents a different level of complexity based on existing knowledge of the Borden sand. These models include: *A*) homogeneous base case scenario; *B*) the inclusion of a single layer with no air-entry pressure change; *C*) a single layer with an air-entry pressure contrast with the surrounding aquifer; and *D*) a layer with an air-entry pressure change with a 1 m discontinuity centred 2.5 m down-gradient of the injectors. A summary of the parameters used to inform each scenario is provided in Table 1.

3.2 Electrical Resistivity Tomography

3.2.1 Electrical Conductivity

The conduction of electrical currents in soil is controlled by several mechanisms, including: electrolytic conduction (Friedman, 2005), ohmic conduction (Robinson and Coruh, 1988), and interfacial conduction (Ruffet et al., 1995). In sandy sediment, electrical current flow is primarily controlled by electrolytic conduction. In fully or partially saturated soils, the pore water and the geometry of the pore space (e.g., connectivity, pore throat size, etc.) will control the bulk electrical conductivity of the medium. The conductivity of partially saturated porous media can be approximated by an empirical equation known as Archie's Law:

$$\sigma = \frac{\phi^m S_w^n}{a} \sigma_w, \qquad [1]$$

where σ is the bulk conductivity of the medium (S/m), S_w is water saturation (-), ϕ is porosity of the soil (-), σ_w is conductivity of the pore fluid (S/m). Variables *a*, *m* and *n* are empirical fitting parameters which account for the pore size, shape, and fluid distribution. The saturation exponent, *n*, depends on the pore fluid but typically has a value of 2 (Archie, 1942). The cementation exponent, *m*, represents the level of cementation in the porous medium, and typically has a value of 1.3 – 2.6 (Doveton, 1986). The tortuosity factor, *a*, has a range of values from 1 – 2 (Attia, 2005). The conductivity of the pore fluid depends on a number of factors such as the ionic composition of the pore fluids (Jorgensen, 1996) and temperature (Ma et al., 2011). These effects can alter the conductivity of the pore fluid by several orders of magnitude.

3.2.2 ERT Model Implementation and Analysis

Res2DMod (version 3.01) was used to compute the ERT response to gas migration in the aquifer. Res2DMod uses a finite-difference formulation to solve Ohm's Law and a conservation of charge (Dey and Morrison, 1976; Loke, 2002). Hydrological models were converted to an equivalent electrical resistivity ($1/\sigma$) distribution of the subsurface. Each geoelectrical model

was discretized using 29 rows of blocks which increased geometrically in size with depth, such that at surface the blocks were 0.1 m tall and the deepest blocks were 0.8 m tall. Each block was 0.25 m wide. The ERT model domain ran from 23 m up-gradient of the injectors to 24 m downgradient of the injectors and went from surface to a depth of 10 m bgs. The saturation values of each block were determined by averaging the saturations from the flow model cells within each ERT model block, as was porosity. A portion of the modelled zone in the ERT extended outside of the domain of the groundwater flow model. The saturation and porosity of the cells in these regions were based on the values encountered along the right and left edges of the flow model domain.

Equation 1 was used to determine the resistivity ($1/\sigma$) of each cell of the ERT model. The empirical parameters and resistivity of water used were: a = 1 (Archie, 1942), m = 1.3 (Doveton, 1986), n = 1.6 (Mickle, 2005), and ρ_w = 1/0.0482 S/m = 20.75 Ωm (Cahill et al., 2017). For this study, it is assumed that injected gas will displace the pore fluid, causing a reduction in the water saturation and remain relatively insoluble during the 72-day injection period, thus electrical conductivity of the pore water should remain stable (Kaye and Laby, 1995). This relative insolubility implies that the water saturation term is the only variable in Equation 1 that changes during the injection period.

Once these values were determined all the resistivity values were grouped into sixteen distinct values using k-means clustering and the distribution of these values was saved in a format readable by Res2DMod. Sixteen resistivity values represent the maximum number of resistivity units that can be modelled using this program. A 48 electrode dipole-dipole survey with an electrode spacing of 1.0 m was then simulated for each model as per the field experiment (Steelman et al., 2017); each forward model consisted of 32 different electrode spacings; 3%

noise was added to the apparent resistivity values of the forward modelled data. Following the forward modelling process, the output of the resistivity model was inverted using Res2DInv (Version 3.59) (Geotomo Software, Malaysia). The vadose zone response was often very large, so for clarity, data shallower than 1 m was muted as were the resistivities outside the flow model domain.

3.2 Ground-Penetrating Radar

3.2.1 Dielectric Permittivity

Dielectric permittivity is the degree to which a material polarizes in the presence of an electrical field, which impacts the ability of the material to form an electric field. This value is typically presented in terms of the relative dielectric permittivity (κ); that is, the dielectric permittivity of a medium relative to the dielectric permittivity of a vacuum ($\varepsilon/\varepsilon_0$), where $\varepsilon_0 = 8.854\times10^{-12}$ F/m (Walker, 2011). Since the dielectric permittivity of all media is greater than that of a vacuum, the relative dielectric permittivity will be greater than 1 for all materials.

In a multi-component soil the bulk dielectric permittivity of the medium can be estimated using a general volumetric mixing model (Tsui and Matthews, 1997):

$$\kappa_T^\alpha = \sum_i \theta_i \kappa_i^\alpha, \qquad [2]$$

where κ_T is the dielectric permittivity of the composite medium (-), θ_i is the volume fraction of the i^{th} component (-); κ_i is the dielectric constant of the i^{th} component (-); and α is a constant that accounts for the grain orientation relative to the electromagnetic field (Roth et al., 1990). The value of α is between -1 and 1 but is taken to be 0.5 for most geologic applications (Knight, 2001); this case is called the complex refractive index model (CRIM). Water, the most common

pore fluid, has a κ = 80.36 at 20 °C, but varies with temperature (Roth et al., 1990), while gasses have a dielectric permittivity of approximately 1 (Davis et al., 1989).

Changes in the dielectric permittivity can be detected in two ways: changes in the velocity of an electromagnetic (EM) wave propagating through the medium and amplitude of reflected energy off a boundary separating two zones of dielectric permittivity (Everett, 2013). The velocity (v) of an EM wave in a low-loss medium is given by:

$$v = \frac{c}{\sqrt{\kappa}}, \qquad [3]$$

where c is the EM velocity in free space and κ is the relative dielectric permittivity of the medium. When a wave travels across an interface between materials with different permittivity, a portion of the energy is reflected back to surface (Everett, 2013). The amount of reflected energy is proportional to the square of the reflection coefficient, R, a measure of the amplitude of the reflected wave relative to the incident wave. For a wave travelling perpendicular to a dielectric boundary, the reflection coefficient is defined as:

$$R = \frac{\sqrt{\kappa_2}-\sqrt{\kappa_1}}{\sqrt{\kappa_2}+\sqrt{\kappa_1}}, \qquad [4]$$

where κ_1 and κ_2 are the dielectric constants of the incident and refracting media, respectively. Equation 4 shows that as the contrast between the dielectric permittivity in the two materials increases the amplitude of the reflected wave also increases. Therefore, a reduction in water saturation associated with gas imbibition above or below a reflecting interface would lead to an increase in EM wave velocity and the amplitude of the signal returned to surface. This implies that when a wave travels through the zone of gas accumulation, it will travel faster, causing the event to arrive earlier and with a higher relative amplitude in a radar section.

3.2.2 GPR Model Implementation and Analysis

ReflexW (Version 8.2.2) was used to model the forward GPR response to gas-phase distribution in the aquifer. ReflexW uses a finite-difference formulation to solve Maxwell's Equations (Sandmeier, 2017). The gas distribution was used to determine the dielectric permittivity (κ) and electrical conductivity (σ); these values were calculated for each node in the groundwater flow model. Each cell was considered to have three components: mineral, pore water, and gases (i.e., air and methane). Literature values were used to determine the κ values for each component; solids were assumed to be quartz grains $\kappa = 4.2$ (Keller, 1987) and gases were assumed to be comparable to a vacuum $\kappa = 1$ (Everett, 2013). Using a groundwater temperature of 10°C (Steelman et al., 2017) the dielectric permittivity of water was calculated to be $\kappa = 84.9$ (Roth et al., 1990). The volumetric components were determined using the porosity and simulated water saturations. Similarly, σ was determined using Equation 1 using the same empirical parameters and water conductivity value used in the ERT model. The values for κ and σ were considered to be point measurements taken at the center of the node.

Both 1D and 2D models were computed for each of the four selected cases. Firstly, full 2D GPR profiles within the hydrogeologic model domain were computed for specific days of the simulation period (i.e., Days 0, 20, 37, 56, 71, and 102). In these models, a GPR trace response was recorded every 0.1 m along the ground surface, beginning with the transmitter and receiver centred at -6 m (i.e., 6 m up-gradient) and ending with the receiver centred at 10 m down-gradient relative to the injectors. This resulted in a 16 m long reflection profile centred within the 20 m wide flow model domain. The second set of models consisted of 1D traces at three positions within the model domain (i.e., -1.5 m, 2.5 m, 6.5 m relative to the position of the

injectors); for these cases a forward GPR response was computed for each day of the simulated period (i.e., Days 0 through 102).

Models were computed using a point source 200 MHz Ricker wavelet. The GPR response was measured with a time step of 0.1 ns with a total time window of 300 ns using a fixed 0.5 m antenna separation. Excitation and registration occurred normal to the survey line (representing a typical antenna configuration in the field) utilizing linear absorbing boundaries along the edges of the model domain to reduce boundary effects. The model was discretized on a 0.025 m grid, linearly interpolating κ and σ between points.

For each trace, a gain function was applied to account for signal attenuation, while a bandpass filter was applied to reduce high frequency noise or signal scattering effects. The envelope of the GPR amplitude was calculated for each time-lapse trace to evaluate changes in the amount of energy reflected to surface relative to background conditions over the time (e.g., relative to Day 0).

GPR traces were assembled into either reflection profiles (i.e., a 2D snapshot of the flow model domain on a given day from 0 to 300 ns) or a time-series plot of enveloped signal amplitude at three locations over the model domain. The sum of the enveloped amplitude was calculated from 50 to 150 ns to determine relative changes in reflected energy over the course of the injection roughly corresponding to depths of 1.5 m bgs to 4.5 m bgs assuming a constant EM wave velocity of 0.06 m/ns.

4.0 Results

4.1 Methane Gas Migration Scenarios

The base case where methane gas is injected into a uniform aquifer (*Scenario A; Table 1*) showed that the gas migrated vertically under buoyancy (Figure 3). As the gas migrated vertically it spread in the horizontal direction creating a plume that was thin near the source and wide where it vented into the vadose zone. The gas migrates upwards once the pressure gradients and buoyant forces exceed the hydrostatic pressure of the overlying water column; lateral spreading is enhanced by increased pressure (i.e., injection rate) at the leakage points observed in Day 37 and 56.

When a layer was added to the aquifer between 3.0 and 3.5 m bgs (*Scenario B; Table 1*), lateral gas migration was enhanced in both the up- and down-gradient direction with consistently higher gas saturations within and below the layer relative to the uniform case (Figure 3). At lower injection rates (i.e., Phases I – III; Days 0 – 70), the gas spread up- and down-gradient along the base of the layer before migrating vertically through the layer toward the vadose zone. At higher injection rates (i.e., Phase IV; Day 70 – 72), the gas further expanded along the base but did not establish a clear preferential pathway vertically to the vadose zone. Once the gas entry pressure of the layer was increased (*Scenario C; Table 1*) a reduction in the gas saturation within the layer was observed (Figure 3). This was accompanied by a further enhancement in lateral spreading of gas, and earlier and more frequent occurrences of vertical preferential gas pathways to the vadose zone. The presence of a 1 m discontinuity in the layer positioned 2.5 m downgradient from the two injectors (*Scenario D; Table 1*) led to the formation of well-defined gas hotspot that channelled gas into the vadose zone (Figure 3) like *Scenario C*. Nevertheless, a portion of the gas managed to migrate horizontally past the discontinuity, thereby sustaining the formation of laterally extensive gas plume in an aquifer characterized by sedimentary layers of finite lateral extent.

4.2 Electrical Resistivity Tomography Response

Scenario A: Homogenous Aquifer

Electrical resistivity tomography (ERT) in a homogenous subsurface showed an anomalous rise in the electrical resistivity over the course of the injection that roughly approximated the location of the main gas plume. Figure 4 shows the electrical response on Day 56. Here, a resistivity increase corresponds to a reduction in the pore water within the aquifer material. Slater et al. (2007) reported similar results when observing the resistivity of an ex-situ peat block, whereby methanogenesis within the peat (i.e., methane gas formation) caused an increase in the electrical resistivity.

While the most apparent response seen by ERT was an increase in resistivity, small decreases, implying increasing water saturation, were also observed. Although Doetsch et al. (2015) observed decreases in resistivity during a gas-phase carbon dioxide injection these were caused by alterations in groundwater chemistry associated with the presence of dissolved carbon dioxide. Since chemical degradation and biological reactions were not incorporated in the gas flow modelling, changes in groundwater chemistry were not accounted for; thus, any decreases in resistivity can be attributed to the 3% noise added to the forward model or inversion artefacts.

Gas saturation estimates from the change in resistivity show similar saturation values near surface. At greater depths, the predicted saturation distributions from the ERT begin to differ from the simulated distribution; the predicted saturation distribution is wider than the true gas distribution at the shallow injector, and there is no observed response in the calculated saturation at the deeper injector. The parabolic shape described by (Thomson and Johnson, 2000) is also

not well-defined by the resistivity response; instead the response describes a box-like distribution with an equal width.

Saturation estimates derived from the ERT data begins to approximate the true saturation near surface. The width of the hotspot, where methane is released to the vadose zone is reasonably well-represented by the ERT data, suggesting that ERT may be useful for estimating the gross volume of methane in the subsurface and identifying the position of hotspots. However, the utility of ERT to estimate gas saturations will depend on the accuracy of fitting parameters in Archie's Equation, which typically requires calibration to specific site conditions.

Scenario B: Aquifer with a Layer

A large zone of increased resistivity is shown roughly in the center of the methane plume, as illustrated by the response on Day 56 (Figure 4). Again, the change in resistivity approximates the shape of the plume around the shallow injector with diminished agreement deeper in the aquifer. Despite the similarity in the resistivity responses between the homogeneous and heterogeneous cases, this case highlights some limitations in using ERT to estimate distributions in gas saturation. The central chimney in the layer case is much thinner than the width of the central chimney predicted by the resistivity data. Furthermore, the small preferential pathways (e.g., up-gradient) are not resolved by ERT.

Scenario C: Layer with Adjusted Entry Pressure

As in both previous cases, the ERT response ably captures the bulk gas migration in the shallow subsurface, but becomes more limited with depth, showing no response around the deep injector (Day 56 shown in Figure 4). Here, the inability to detect thin features becomes even more apparent, as lateral migration in thin pools extends quite far in the up- and down-gradient

directions and is not discernible from the ERT response. The primary gas bulb emanating from the injectors is reasonably well-defined by the central resistivity response; however, the establishment of more complex vertical gas pathways up- and down-gradient are not imaged in the ERT model. It should be noted that the position of multiple vertical pathways observed up-gradient coincides with a zone of high resistivity along the water table indicating possible detection of gas efflux into the vadose zone.

Scenario D: Discontinuous Layer

The presence of a discontinuity within the low-permeable layer (i.e., Day 56 shown in Figure 4) leads to a reduction in the bulk gas saturation below the layer. ERT simulations indicate that the primary response associated with the gas has shifted upward in the profile. These data also show an increase in resistivity slightly down-gradient along the water table interface which corresponds to the formation of a preferential gas pathway through the discontinuity and eventual efflux into the vadose zone.

4.3 Ground-Penetrating Radar Response

Scenario A: Homogeneous Aquifer

Strong reflections in ground-penetrating radar (GPR) data require sharp dielectric boundaries, so little change can be expected in the GPR signal for the homogeneous case (Day 56 shown in Figure 5). However, these data do show a series of diffractions corresponding to the sides of the plume and at the shallow injector point. These diffractions tend to be associated with points marking an abrupt change in dielectric permittivity, such as a small void or discontinuity along a boundary or the gas leakage points. The high gas saturation and steep saturation gradient around the injector resulted in a higher amplitude hyperbola at the base of the plume than along the

sides, where the gas saturation gradient is less extreme. The only notable reflection response in the homogeneous case occurs along the water table, which is demarcated by diminished reflection amplitude along the full extent of the hotspot as the capillary fringe becomes more diffuse. At Day 56 (Figure 5) the water table above the injector nearly disappears from the radar profile, while it is still visible past the extent of the hotspot.

Scenario B: Aquifer with a Layer

When a layer with $k_L = 5.1 \times 10^{-13}$ m^2 and $\phi = 0.31$ is present in the aquifer, a dielectric permittivity contrast forms within the saturated zone resulting in a strong reflection in the GPR profile. A number of diffractions still define the outer boundary of the gas plume, with a strong diffraction occurring at the shallow injector (Day 56 shown in Figure 5). Additionally, the water table reflection disappears over a region marking the location of gas efflux to the vadose zone. While these responses are similar to the homogeneous case, the addition of a layer led to the accumulation of gas, and thus, stronger dielectric permittivity contrasts in the aquifer. A pull-up in the layer's reflection due to higher gas saturations above was also observed. Lassen et al. (2015) observed a similar increase in the velocity of electromagnetic waves using cross borehole GPR during a carbon dioxide injection.

Scenario C: Layer with Adjusted Entry Pressure

When a layer with $k_L = 5.1 \times 10^{-13}$ m^2 and $\phi = 0.31$ is added and the entry pressure is increased to $P_c = 2.99$ kPa the GPR response begins to show more spatial and temporal variability in amplitude compared to the previous homogeneous and layered cases. At Day 56 (Figure 5), the water table reflection demarcating the gas hotspot has effectively disappeared; reflector pull-up is readily visible and is accompanied by ample diffractions associated with the accumulation of

gas along the base of the layer. Unlike the previous cases, the majority of the diffractions (i.e., the bulk of the reflected energy) occur below the layer as the gas distribution above the layer become more diffuse due to the enhanced lateral spreading induced by the layer's higher entry pressure.

Gas plume extension along the base of the layer is more visible in the GPR response compared to the previous scenarios. Here, the sharp boundary formed by the migration of methane creates an ideal GPR target for the detection of gas in the formation, especially in areas where methane migrated in thin pools laterally away from the main plume. This response shows that GPR has the capacity to track the pooling of methane along hydrogeologic boundaries. This observation parallels those of Brewster et al. (1994) who used GPR to monitor DNAPL migration in the Borden aquifer. However, in their case the fluid was denser than water and moved downwards under gravity and was shown to cascade along a series of discontinuous lenses of lower-permeability sand within the aquifer.

Scenario D: Discontinuous Layer

When a similar layer ($k_L = 5.1 \times 10^{-13}$ m^2, $\phi = 0.31$, $P_c = 2.99$ kPa) with a 1 m discontinuity centred at 2.5 m was introduced the diffractions become less pronounced along the base of the layer; however, additional diffraction events form along the terminus of the layer (i.e., at the edges of the discontinuity; Figure 5). The shift in gas migration toward the down-gradient discontinuity can be associated with a reduction in the reflection amplitude at the location of the discontinuity, together with the occurrence of additional diffractions arising from the upper and lower boundary (terminuses) of the discontinuity. Reduced reflector amplitudes are observed immediately above the injectors as gas preferentially migrates toward and through the layer

discontinuity. Meanwhile, increased reflector amplitudes are observed down-gradient of the discontinuity due to the formation of a thin, higher gas saturation plume.

4.4 ERT and GPR Time-Series

Average electrical resistivity changes for Days 1, 20, 37, 56, 71 and 102, above (1 – 4.5 m bgs) and below (4.5 – 9.0 m bgs) the uppermost injector is shown in Figure 6. Each scenario exhibits a similar systematic increase in resistivity during the active injection phase followed by a reduction to near-background levels post injection. The largest resistivity increase was observed above the shallow injector for all four scenarios. However, differences in resistivity between the two intervals varied during the injection and post injection periods. Shallow and deep resistivity values began diverging through Phase I, reaching their greatest separation during Phase II. The onset of Phase IV (highest injection rate) was accompanied by a temporary convergence of the shallow and deep resistivity before separating once again after the injection re-commenced. Although the inclusion of a lower-permeable layer of varying hydraulic properties had a minor impact on the overall magnitude of the resistivity increase notable differences in the signal was observed. For example, *Scenario B* and *C* both exhibit slightly higher resistivity in the shallower interval, which is consistent with the preferential accumulation of gas below the low-permeable layer (Figure 3); the absence of a layer (*Scenario A*) or the presence of discontinuity in a layer (*Scenario D*) was accompanied by relatively lower resistivity in the shallow interval, which is consistent with more efficient vertical gas migration or lower gas retention. Although ERT provides limited insight into the spatial distribution of gas in the subsurface, these models show that the method is sensitive to gas retained in the aquifer at a macroscale (meters).

In comparison, changes in GPR enveloped energy (i.e., signal amplitude) between 50 and 150 ns at positions -1.5 m, 2.5 m and 6.5 m from the injection horizon (Figure 6) reveal a much more

dynamic response to changes in injection rate for each of the four scenarios. Although a relatively weak amplitude response was observed for the case of a uniform aquifer (*Scenario A*), due to a lack of dielectric contrasts, distinct peaks were observed at the two locations nearest the injector (i.e., -1.5 and 2.5 m) during each rate change; however, signal amplitudes farther downgradient at 6.5 m only responded to the highest leakage rate (Phase IV). The addition of a lower-permeable layer above the shallow injector (*Scenario B*) had a marked impact on the magnitude of the reflectivity particularly following changes in injection rate. Here, the largest peak was observed a few days after the onset of Phase II. Increasing the entry-pressure of the layer (*Scenario C*) further enhanced these reflectivity signals, contributing to a longer-period high-amplitude pulse after each rate change. In this scenario, the most notable difference occurred during Phase I, as each location was marked by a sharp increase in reflectivity within the first few days of the injection followed by a gradual decline until the onset of Phase II. Here, a sharp increase in amplitude was observed at the up-gradient location with a more subdued increase at the two down-gradient locations. Amplitudes show a systematic decline and eventual reduction to near-background levels through the temporary shut-down period. Commencement of Phase II after the shut-down was accompanied by an increase at -1.5 m and 6.5 m, with relatively lower response at 2.5 m. Reflectivity values appear to reach a steady-state condition by Day 55 at all three locations. During Phase III, when the shallow injector was turned off, the two locations close to the injectors (-1.5 m and 2.5 m) exhibited a decrease in amplitude while conditions at 6.5 m remained unaffected. A relatively minor amplitude response was observed during the highest rate period (Phase IV), indicating that signal amplitude is not indicative of the flux or leakage rate in the aquifer. The inclusion of a discontinuity in the layer (*Scenario D*) reveals additional spatial and temporal variations in the reflectivity associated with changes in

gas-phase behaviour (Figure 3). Although GPR amplitudes exhibit little correlation with the actual leakage rates, systematic fluctuations in amplitude following transience in gas-phase behaviour, together with spatial differences in signal amplitude demonstrate its high sensitivity to changes in physical properties, gas-phase dynamics, and flow system geometry.

5.0 Discussion and Conclusions

Geophysical methods have long been a tool used in tracking immiscible-phase fluid migration and distribution, including dense non-aqueous phase liquids and gas-phase constituents. However, the relative utility of ERT and GPR to monitor highly transient gas-phase plumes in an unconfined aquifer, such as a methane leakage event from a series of point sources has not been demonstrated. Although Steelman et al. (2017) reported field observations of ERT and GPR responses during a controlled methane leakage experiment in the Borden aquifer, it was unclear which physical properties of the groundwater flow system were primarily responsible for the laterally extensive and episodic distribution of gas in the subsurface observed by the geophysical techniques and the overall nature of the geophysical signature used to elucidate hydrogeologic dynamics.

Our numerical simulations show that ERT is effective at monitoring macroscale gas accumulation primarily around an injector where gas accumulation would be most significant, which is consistent with recent laboratory experiments using ERT to image CO_2 and N_2 gas circulation (e.g., Kremer et al., 2018). However, our results also indicate that the ERT method will be much less effective at resolving thin pools of gas extending beyond the main bulb. This result is consistent with inherent limitations in electrical resistivity methods, specifically with respect to spatial resolution and depth (Loke et al., 2013). The inability to detect changes at depth could be overcome by increasing the electrode spacing; however, this would come at the

expense of spatial resolution. It should be noted that the height of the model blocks increases with depth, which, when combined with relatively low levels of water desaturation (i.e., increased gas saturations), results in a small response to the bulk resistivity. Similarly, model parametrization could have impacted the detection of thin elements; for instance, lateral discretization in the hydrogeologic modelling was 0.1 m, while in the forward geophysical modelling of the ERT response was computed with a 0.25 m cell size, resulting in a smoothed representation in the actual gas distribution. Further modelling using a more sophisticated forward modelling scheme may yield greater consistency between the gas saturations calculated from the flow model and the inverted geophysical model. Although the modelled ERT response to the gas distribution in the subsurface was only effective at detecting the primary gas bulb, there was some evidence of an electrical response associated with the establishment of vertical preferential pathways farther away. This observation is consistent with Steelman et al. (2017), whose ERT measurements showed both a gas bulb and a thin zone of higher resistivity extending farther down-gradient. However, ERT remains relatively insensitive to gas injection in both the field experiment and modelled scenarios.

As it stands, the modelled scenarios demonstrate that ERT has the capacity to show where gas might be venting to the vadose zone and provide a good qualitative measure of the position of the main plume assuming limited lateral spreading has occurred. However, as the geology becomes more complex, contributing to greater lateral mobility and spreading along thin high gas saturation pools, ERT quickly becomes a less effective imaging tool. The spatially complex distribution together with the numerical simulations indicate that the ERT will be more useful for identifying concentrated zones of methane accumulation or major preferential pathways to the water table or ground surface (e.g., Forde et al., 2019).

In contrast, the GPR was highly sensitive to the accumulation of gas beneath permeability contrasts and responded to a wide range of dielectric contrasts induced by the movement of gas in the subsurface; thin pools beneath capillary barriers extending beyond the limits of the primary gas plume were readily detected by GPR. However, there were some differences between the modelled scenarios and the GPR results of the field experiment (Steelman et al., 2017). The diffractions that defined the edges of the plume in the modelled GPR response (Figure 5; *Scenario B, C and D*) were not readily evident in the field, and no notable pull-up in reflection events was observed during the field experiment. Steelman et al. (2017) also noted that methane migration was primarily down-gradient of the injectors, and potentially travelled farther than that depicted in these simulations. The results of the field experiment are best approximated by the simulated response associated with an increase in the entry pressure at a permeability barrier (*Scenario C/D*). The main difference being that instead of a single layer as depicted in the simulations, the field results reflect the influence of multiple lenses of short lateral extent trapping gas in pockets, thereby contributing to a more complex and spatially distributed increase in signal reflectivity over the active injection period.

The build-up and spill-over of methane from one layer to another, inversely analogous to the patterns of DNAPL migration observed by Brewster and Annan (1994), also showed significant lateral migration; our numerical simulations re-affirm the potential for high lateral mobility of a pressurized methane source in an unconfined aquifer characterized by subtle layering with permeability contrasts with varying capillary pressures. The mix of areas of high and low gas concentrations, together with the spatially variable reflectivity distribution observed during the field experiment (Steelman et al., 2017; Cahill et al., 2018), indicates that methane gas was largely directed through a complex network of interbedded sand layers of variable length scales

acting as preferential pathways. A recent experimental and modeling study by Cihan et al (2018) investigating the role of capillary hysteresis and pore-scale heterogeneity on CO_2 gas migration showed that plume front migration would occur intermittently, with periods of stagnation interrupted by sudden migration bursts; this behaviour appears to be analogous to the sudden lateral methane migration events that occurred irrespective of changes in the injection rate during the field experiment (Steelman et al., 2017). However, capillary hysteresis and pore-scale heterogeneity is beyond the capacity of our multi-phase flow model (CFbio), and thus, was not considered in this study.

This modelling was completed under the assumption that the bulk hydraulic properties of soil would adequately describe the movement of methane gas in the aquifer, and that the resulting models would be sufficient to evaluate the geophysical responses associated with gas migration and behaviour in the aquifer. Although the scenarios used to evaluate the geophysical response to methane migration represent idealized conceptualizations, they demonstrate the importance of heterogeneity (i.e., layers with variable permeability and capillary pressure) on the evolution of a methane gas plume emanating from a wellbore. While other numerical simulations of wellbore leakage in an unconfined aquifer by Roy et al. (2016) have suggested that gas will migrate upwards due to buoyancy along the well casing and eventually escape to the atmosphere, our results show that a gas can migrate a substantial distance laterally due to subtle permeability contrasts consistent with field observations.

A well constrained plume conceptualization hinges on an accurate understanding of the distribution of the gas-phase in the subsurface. Although ERT results were generally consistent with the field experiment, the numerical simulations confirm that ERT is only moderately effective at characterizing methane leakage from a well, especially if heterogeneity or anisotropy

is contributing to lateral migration along thin layers. Meanwhile, GPR would be a much more effective tool in tracking the migration of gas along preferential pathways, assuming the gas is not constrained to a bulb with limited lateral mobility. The field experiment by Steelman et al. (2017) suggested that both geophysical methods could be applicable in monitoring the evolution and migration of methane plumes depending on the state of the plume's evolution. This modelling, despite its simplicity, does confirm that co-application of these geophysical methods to evaluate the migration and distribution of fugitive methane in unconfined aquifers is tenable, and in combination, strongly complementary. Additional work remains to enhance our understanding of additional chemical and biological processes such as methane oxidation (aerobic and anaerobic) on the geophysical signatures associated with gas and aqueous-phase methane migration at longer time scales. Also, the role of external hydrologic processes (recharge, barometric pressure, and temperature), and more complex physical property conditions (capillary hysteresis and microscale heterogeneity) will enhance the model representation of system characteristics and resultant effects on geophysical signatures associated with gas plume dynamics under field conditions.

Acknowledgements

This research was made possible through an NSERC Strategic Partnerships Grant Project (SPG-P) awarded to Drs. John Cherry and Beth Parker along with their project collaborators Drs. Aaron Cahill, Bernhard Mayer, Ulrich Mayer and Cathryn Ryan. The authors would like to thank Dr. Ken Walton for their technical support and guidance on the use of CFbio, and the two anonymous reviewers for their constructive feedback.

References

Archie, G.E., 1942. The electrical resistivity log as an aid in determining some reservoir characteristics. *In* Petroleum technology (pp. 54–62). Dallas, TX.

Atekwana, E.A., Atekwana, E.A., 2010. Geophysical signatures of microbial activity at hydrocarbon contaminated sites: A review. Surv. Geophys. 31, 247 – 283. doi: 10.1007/s10712-009-9089-8.

Attia, A.M., 2005. Effects of petrophysical rock properties on tortuosity factor. J. Pet. Sci. Eng. 48, 185–198. doi: 10.1016/j.petrol.2005.06.012.

Binley, A., Hubbard, S.S., Huisman, J.A., Revil, A., Robinson, D.A., Singha, K., Slater, L., 2015. The emergence of hydrogeophysics for improved understanding of subsurface processes over multiple scales. Water Resour. Res. 51. doi: 10.1002/2015WR017016.

Boaga, J., 2017. The use of FDEM in hydrogeophysics: a review. J. Appl. Geophys. 139, 36–46. http://dx.doi.org/10.1016/j.jappgeo.2017.02.011

Brewster, M.L., Annan, A.P., 1994. Ground-penetrating radar monitoring of a controlled DNAPL release: 200 MHz radar. Geophysics 59, 1211–1221.

Brewster, M.L., Annan, A.P., Greenhouse, J.P., Kueper, B.H., Olhoeft, G.R., Redman, J.D., Sander, K.A., 1995. Observed migration of a controlled DNAPL release by geophysical methods. Groundwater 33, 977–987.

Das, B.M., 2008. Advanced Soil Mechanics (3rd edition). New York, NY. doi: 10.1029/EO066i042p00714-02.

Davis, J.L., Annan, A.P., 1989. Ground-penetrating radar for high-resolution mapping of soil and rock stratigraphy. Geophys. Prospect. 39, 531–551. doi: 10.1111/j.1365-2478.1989.tb02221.x

Doetsch, J., Fiandaca, G., Auken, E., Christiansen, A.V., Cahill, A.G., Jakobsen, R., 2015. Field-scale time-domain spectral induced polarization monitoring of geochemical changes induced by injected CO2 in a shallow aquifer. Geophysics 80, WA113–WS126. doi: 10.1190/geo2014-0315.1

Doveton, J.H., 1986. Log analysis of subsurface geology: Concepts and computer methods. John Wiley and Sons, Inc.

Cahill, A.G., Beckie, R., Ladd, B., Sandl, E., Goetz, M., Chao, J., Soares, J., Manning, C., Chopra, C., Finke, N., Hawthorne, I., Black, A., Mayer, K.U., Crowe, S., Cary, T., Lauer, R., Mayer, B., Allen, A., Kirste, D., Welch, L., 2018. Advancing knowledge of gas migration and fugitive gas from energy wells in northern British Columbia, Canada. Greenhouse Gas Sci Technol. 00, 1 – 18. doi: 10.1002/ghg

Cahill, A.G., Steelman, C.M., Forde, O., Kuloyo, O., Ruff, E., Mayer, B., Mayer, K.U., Strous, M., Ryan, M.C., Cherry, J.A., Parker, B.L., 2017. Mobility and persistence of methane in

groundwater in a controlled release field experiment. Nat. Geosci.10, 289 – 294. http://dx.doi.org/10.1029/2007JG000575.

Cahill, A.G., Parker, B.L., Mayer, B., Mayer, K.U., Cherry, J.A., 2018. High resolution spatial and temporal evolution of dissolved gases in groundwater during a controlled natural gas release experiment. Sci. Total Environ. 622-623, 1178–1192. https://doi.org/10.1016/j.scitotenv.2017.10.049

Cihan, A., Wang, S., Tokunaga, T.K., Birkholzer, J.T., 2018. The role of capillary hysteresis and pore-scale heterogeneity in limiting the migration of buoyant immiscible fluids in porous media. Water Resour. Res. 54. https://doi.org/10.1029/2018WR022741.

Council of Canadian Academies, 2014. Environmental Impacts of Shale Gas Extraction in Canada. Ottawa (ON): The Expert Panel on Harnessing Science and Technology to Understand the Environmental Impacts of Shale Gas Extraction. Council of Canadian Academies.

Everett, M.E., 2013. Near-surface applied geophysics. Cambridge: Cambridge University Press.

Daily, W., Ramirez A., 1995. Electrical resistance tomography during in-situ trichloroethylene remediation at the Savannah River Site. J. Appl. Geophys. 33, 239–249.

Dey, A., Morrison, H., 1976. Resistivity modeling for arbitrarily shaped two-dimensional structures. Geophysics 41, 62. doi: 10.1190/1.1440608.

Forde, O.N., Mayer, K.U., Cahill, A.G., Mayer, B., Cherry, J.A., Parker, B.L., 2018. Vadose zone gas migration and surface effluxes following a controlled natural gas release into an unconfined shallow aquifer. Vadose Zone J. 17, 180033. doi: 10.2136/vzj2018.02.0033.

Forde, O.N., Mayer, K.U., Hunkeler, D., 2019. Identification, spatial extent and distribution of fugitive gas migration on the well pad scale. Sci. Total Environ. 652, 356–366. https://doi.org/10.1016/j.scitotenv.2018.10.217

Friedman, S.P., 2005. Soil properties influencing apparent electrical conductivity: A review. Comput. Electron. Agric. 46, 45 – 70. doi: 10.1016/j.compag.2004.11.001.

Harvey, T., Arnaud, E., Meyer, J.R., Steelman, C.M., Parker B.L. (accepted) Characterizing scales of hydrological heterogeneity in ice marginal sediments, Wisconsin USA, Hydrogeology J. Submitted: 25-Oct-2018, HJ-2018-5691.

Hwang, Y.K., Endres, A.L., Piggott, S.D., Parker, B.L., 2008. Long-term ground penetrating radar monitoring of a small volume DNAPL release in a natural groundwater flow field. J. Contam. Hydrol. 97, 1–12. doi: 10.1016/j.jconhyd.2007.11.004.

Jorgensen, D.J., 1996. The ratio method of estimating water resistivity and TDS from resistivity logs. Groundwater 34, 519–522.

Kaye, G.W.C, Laby, T.H., 1995. Tables of physical and chemical constants (16^{th} ed.) Essex, England: Longman Group Limited

Keller, G.V., 1987. Rock and Mineral Properties. *In* Nabighian, M.N. (Ed.), Electromagnetic methods in applied geophysics – theory: Volume 1 (pp. 13–51. Tulsa, OK. Society of Exploration Geophysicists.

Knight, R., 2001. Ground penetrating radar for environmental applications. Annu. Rev. Earth Planet. Sci. 29, 229–255. https://doi.org/10.1146/annurev.earth.29.1.229

Knight, R., Pyrak-Nolte, L.J., Slater, L., Atekwana, E., Endres, A., Geller, J., Lesmes, D., Nakagawa, S., Revil, A., Sharma, M.M., Straley, C., 2010. Geophysics at the interface: Response of geophysical properties to solid-fluid, fluid-fluid, and solid-solid interfaces. Rev. Geophys. 48, RG4002. doi: 10.1029/2007RG000242.

Kremer, T., V. Cristian, Maineult, A., 2018. ERT monitoring of gas injection into water saturated sands: modelling and inversion of cross-hole laboratory data. J. Appl. Geophys. 158, 11–28, http://doi.org/10.1016/j.jappgeo.2018.06.001.

Kueper, B.H., Frind, E.O., 1991. Two-phase flow in heterogeneous porous media: 2. Model application. J. Contam. Hydrol. 2, 95–110.

Lassen, R.N., Plampin, M., Sakaki, T. Illangasekare, T.H., Gudbjerg, L., Sonnenborg, T.O., Jensen, K.H., 2015. Effects of geologic heterogeneity on migration of gaseous CO2 using laboratory and modelling investigations. Int. J. Greenh. Gas Control 43, 213 – 224. http://dx.doi.org/j.ijggc.2015.10.015

Loke, M.H., 2002. Rapid 2D resistivity forward modelling using the finite-difference and finite-element methods. International Immunology 25, 28.

Loke, M.H., Chambers, J.E., Rucker, D.F., Kuras, O., Wilkinson, P.B., 2013. Recent developments in the direct current geoelectrical imaging method. J. Appl. Geophys. 95, 135–156, http://dx.doi.org/10.1016/j.jappgeo.2013.02.017.

Ma, R., McBratney, A., Whelan, B., Minasny, B., Short, M., 2011. Comparing temperature correction models for soil electrical conductivity measurements. Precis. Agric. 12, 55–66. doi: 10.1007/s11119-009-9146

Meyer, J.R., Parker, B.L., Arnaud, E., Runkel, A.C., 2016. Combining high resolution vertical gradients and sequence stratigraphy to delineate hydrogeologic units for a contaminated sedimentary rock aquifer system. J. Hydrol. 534, 505–523. http://dx.doi.org/10.1016/j.jhydrol.2016.01.015

Mickle, R.J., 2005. A coupled hydrogeological-petrophysical analysis of geophysical variation in the vadose zone, M.Sc. University of Waterloo, Waterloo.

Moortgat, J., Schwartz, F.W., Darrah, T.H., 2018. Numerical modeling of methane leakage from a faulty natural gas well into fractured tight formations. Groundwater, 1–13. doi: 10.1111/gwat.12630

Osborn, S.G., Vengosh, A., Warner, N.R., Jackson, R.B., 2011. Methane contamination of driking water accompanying gas-well drilling and hydraulic fracturing. Proc. Natl. Acad. Sci. U. S. A. 108, E665–E666. doi: 10.1073/pnas.1109270108.

Perrodon, A., 1983. Dynamics of oil and gas accumulation. Pau, France: Elf Aquitaine.

Robinson, E.S., Coruh, C., 1998. Basic Exploration Geophysics. John Wiley and Sons, Inc.

Roth, K., Schulin, R., Fluhler, H., Attinger, W., 1990. Calibration of time domain reflectometry for water content measurement using a composite dielectric approach. Water Resour. Res 26, 2267 – 2273.

Royal Society, 2012. Shale Gas Extraction in the UK: A Review of Hydraulic Fracturing. Issued: June 2012DES2597. The Royal Society and The Royal Academy of Engineering.

Ruffet, C., Darot, M., Guéguen, Y., 1995. Surface conductivity in rocks: a review. Surv. Geophys. 16, 83–105. doi: 10.1007/BF00682714.

Schout, G., Hartog, N., Hassanizadeh, S.M., Griffioen, J., 2018. Impact of an historic underground gas well blowout on the current methane chemistry in a shallow groundwater system. Proc. Natl. Acad. Sci. U. S. A. 115, 296–301. doi: 10.1073/pnas.1711472115.

Slater, L., Comas, X., Ntarlagiannis, D., Moulik, M.R., 2007. Resistivity-based monitoring of biogenic gases in peat soils. Water Resour. Res. 43, 1–13. doi: 10.1029/2007WR006090.

Steelman, C.M., Klazinga, D.R., Cahill, A.G., Endres, A.L., Parker, B.L., 2017. Monitoring the evolution and migration of a methane gas plume in an unconfined sandy aquifer using time-lapse GPR and ERT. J. Contam. Hydrol. 205, 12 – 24. http://dx.doi.org/10.1016/j.jconhyd.2017.08.011.

Sudicky, E.A., Illman, W.A., 2011. Lessons learned from a suite of CFB Borden Experiments. Groundwater 49, 630–648. doi: 10.1111/j.1745-6584.2011.00843.x

Thomson, N.R., Johnson, R.L., 2000. Air distribution during in situ air sparging: an overview of mathematical modeling. J. Hazard. Mater. 72, 265–282.

Tsui, F., Matthews, S.L., 1997. Analytical modelling of the dielectric properties of concrete for subsurface radar applications. Constr. Build. Mater. 11, 149 – 161.

Vidic, R.D., Brantley, S.L., Vandenbossche, J.M., Yoxtheimer, D., Abad, J.D., 2013. Impact of shale gas development on regional water quality. Science 340, 1235009 – 1235009. http://www.sciencemag.org/cgi/doi/10.1126/science.1235009

Tables

Table 1. Hydrogeologic parameters used for multi-phase flow simulations.

Scenario Parameters	**A** Homogeneous Aquifer	**B** Low Permeable Layer	**C** Increased Layer Entry Pressure	**D** Layer Discontinuity
k_h/k_v	10	10	10	10
$k_{h,\,aq}$	2.2×10^{-12} m^2	2.2×10^{-12} m^2	2.2×10^{-12} m^2	2.2×10^{-12} m^2
$k_{h,\,L}$	n/a	5.1×10^{-13} m^2	5.1×10^{-13} m^2	5.1×10^{-13} m^2
ϕ_{aq}	0.33	0.33	0.33	0.33
ϕ_L	n/a	0.31	0.31	0.31
$P_{c,\,aq}$	2.22 kPa	2.22 kPa	2.22 kPa	2.22 kPa
$P_{c,\,L}$	N/A	2.22 kPa	2.99 kPa	2.99 kPa
Discontinuity	n/a	n/a	n/a	1 m wide at 2.5 m

Figure Captions

Figure 1. Multi-phase flow model conceptualizations of the injection experiment used to investigate the response of electrical resistivity and ground-penetrating radar to gas phase dynamics within an unconfined aquifer. Each scenario represents an increase in model complexity relative to the based case (i.e., Scenario A).

Figure 2. Simulated gas injection based on the field experiment of Cahill et al. (2017). A total of 48.7584 m^3 of methane gas was injected into the aquifer for each scenario.

Figure 3. Multi-phase flow model simulations for Days 20, 37 and 56 for the four model scenarios. Changes in gas saturation <5% were ignored.

Figure 4. Relative change in resistivity based on modelled gas phase distributions (upper) with corresponding calculated gas saturations on Day 56 using Eqn. 1 (lower). The black dotted line delineates the lateral extent of the gas phase plume for saturations >5% (refer to Day 56 in Figure 3).

Figure 5. Calculated dielectric permittivity distribution on Day 56 based on gas phase saturation (Eqn. 2) with corresponding forward GPR response. Additional GPR model simulations (Days 0 through 102) were conducted for select trace locations (i.e., -1.5, 2.5 and 6.5 m) for each model scenario; these cumulative amplitudes observed between 50 and 150 ns are provided in Figure 6.

Figure 6. Geophysical response to gas-phase migration for the four model scenarios over the 102 day simulation period: (A) homogeneous and anisotropic aquifer; (B) low permeable layer; (C) layer with increase entry pressure; (D) discontinuous layer. Integrated normalized enveloped GPR amplitude between 50 ns and 150 ns are provided for three positions (i.e., -1.5, 2.5, and 6.5 m) along the hydrogeologic model domain (refer to Figure 5). Average change in resistivity between 1 – 4.5 m bgs (shallow) and 4.5 – 9.0 m bgs (deep) across the model domain are reported for Days 1, 20, 37, 56, 71 and 102 of the simulation period.

HIGHLIGHTS

- Heterogeneity and anisotropy will result in extensive lateral gas migration
- ERT is most effective at monitoring macroscale gas accumulation near source
- GPR detected accumulation of gas beneath subtle permeability contrasts
- Geophysical dynamics were most sensitive to changes in gas entry pressure